

PASTA: Towards Flexible and Efficient HDR Imaging Via Progressively Aggregated Spatio-Temporal Alignment

Xiaoning Liu¹, Ao Li¹, Zongwei Wu², Yapeng Du¹, Le Zhang¹,
Yulun Zhang³, Radu Timofte^{2,4}, and Ce Zhu¹

¹ University of Electronic Science and Technology of China

² University of Würzburg

³ Shanghai Jiao Tong University

⁴ ETH Zurich

Abstract. Leveraging Transformer attention has led to great advancements in HDR deghosting. However, the intricate nature of self-attention introduces practical challenges, as existing state-of-the-art methods often demand high-end GPUs or exhibit slow inference speeds, especially for high-resolution images like 2K. Striking an optimal balance between performance and latency remains a critical concern. In response, this work presents PASTA, a novel Progressively Aggregated Spatio-Temporal Alignment framework for HDR deghosting. Our approach achieves effectiveness and efficiency by harnessing hierarchical representation during feature distanglement. Through the utilization of diverse granularities within the hierarchical structure, our method substantially boosts computational speed and optimizes the HDR imaging workflow. In addition, we explore within-scale feature modeling with local and global attention, gradually merging and refining them in a coarse-to-fine fashion. Experimental results showcase PASTA’s superiority over current SOTA methods in both visual quality and performance metrics, accompanied by a substantial 3-fold ($\times 3$) increase in inference speed.

Keywords: High Dynamic Range Imaging · Hierarchical Representation · Progressive Aggregation

1 Introduction

Imaging sensors’ limited dynamic range often compromises photo quality by losing detail in highlights and shadows. Multi-frame HDR imaging, which involves capturing a stack of low dynamic range (LDR) images at different exposures and then combining them, addresses this by expanding the dynamic range and enhancing visual quality. However, this technique faces challenges in accurately aligning frames in the presence of movement and shake, as well as effectively merging frames of varying exposures while dealing with occlusion.

Recent advancements in HDR imaging have evolved from early methods using hand-crafted features [17, 18, 21, 32, 37, 47] to contemporary learning-based

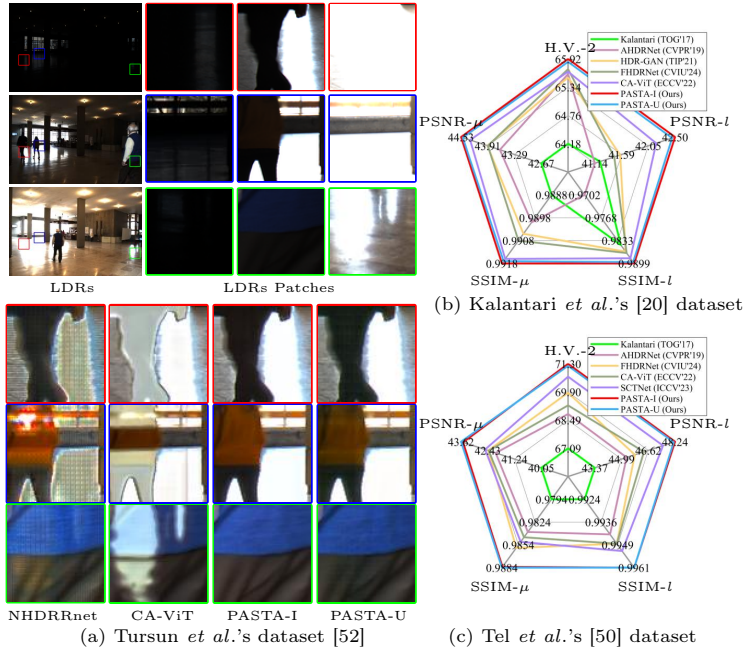


Fig. 1: Visual and quantitative comparison. Our method consistently outperforms in two benchmark HDR datasets, surpassing the state-of-the-art CA-ViT [31] and NHDRNet [60] (the hierarchical method) methods in preserving content integrity, achieving ghost-free and high-fidelity results. Zoom in to see more details.

Table 1: Components in existing HDR deghosting methods. Components are categorized by functionality: i) *Alignment* involves the spatial transformation of misaligned images or features, including homography transformation (HT), spatial attention (SA), pyramid cross attention (PCA), patch aggregation (PC) and temporal attention (TA); ii) *Aggregation* characterizes the architecture of feature aggregation; iii) *Domain* specifies aggregation in either the spatial or frequency domain, and iv) *High Resolution (HR)* refers to the capability to handle 2K images.

	CNN-based Methods				Transformer-based Methods					
	DeepHDR [57] (ECCV'18)	AHDRNet [59] (CVPR'19)	HDR-GAN [38] (TIP'21)	FHDRNet [5] (CVIU'24)	CA-ViT [31] (ECCV'22)	Joint-HDRNet [28] (CVPR'23)	HyHDRNet [58] (CVPR'23)	SCTNet [50] (ICCV'23)	PASTA-I (Ours)	PASTA-U (Ours)
Alignment	Yes (HT)	Yes (SA)	No	No	Yes (SA)	Yes (PCA)	Yes (PC & SA)	No	Yes (TA)	No
Aggregation	Hierarchical	Plain	Hierarchical	Hierarchical	Plain	Plain	Plain	Plain	Hierarchical	Hierarchical
Domain	Spat.	Spat.	Spat.	Freq.	Spat.	Spat.	Spat.	Spat.	Spat. & Freq.	Spat. & Freq.
HR (2K)	Yes	No	Yes	Yes	No	No	No	No	Yes	Yes

models. These models excel in cross-exposure mappings due to inductive bias [20, 24, 35, 57, 59, 60], with Transformer models further enhancing HDR imaging by introducing contextualized awareness [28, 31, 48, 50, 58].

Despite these advancements, a major hurdle is the rising computational complexity with higher image resolutions. The self-attention mechanism in Transformers requires significant computational resources and memory, limiting their real-world applicability, especially with the common use of high-resolution images. While methods like [42, 49] can process 2K images, this often comes at the expense of performance.

This necessitates further reflection and reevaluation of HDR deghosting methods, aiming to construct a simple, powerful and efficient framework. Our sum-

maries, detailed in Tab. 1, distill the methodology into four key components: *Alignment*, *Aggregation*, *Domain*, and *High Resolution*, each critical to the practical effectiveness of HDR deghosting approaches.

We discern that hierarchical representation presents a natural solution capable of simultaneously addressing multiple challenges. This representation inherently contains information from different levels, making it a robust candidate for our objectives. Moreover, hierarchical representation coupled with diverse granularities aligns well with computational efficiency, further enhancing its appeal for our purposes. Motivated by these considerations, we propose a novel framework named Progressively Aggregated Spatio-Temporal Alignment (PASTA) designed to fully exploit the benefits of hierarchical representation for HDR imaging. Inspired by the effectiveness of wavelet statistical modeling [4], we utilize the discrete wavelet transform (DWT) [33] to establish a hierarchical representation framework. Although DWT is commonly employed in various low-level vision tasks [5, 45, 64], prior works predominantly focus on utilizing it to compute frequency-domain features and just perform image-frequency fusion, overlooking the statistical correlation of wavelet coefficients. In contrast, we innovatively incorporate channel attention and spatial self-attention to implicitly capture inter- and intra-scale relationships among subbands. Our approach explores the potential of DWT as a hierarchical representation, offering advantages such as inter-/cross-scale interactions, flexibility, improved computational efficiency and suitability, which is the first time addressed for high-resolution HDR deghosting.

Still, an additional challenge emerges: how to efficiently extract the most informative features and establish cross-hierarchy interactions for effective fusion of all available information. To meet this challenge, we devise a gradual fusion strategy. Initially, we undertake an in-depth analysis incorporating global and local attention mechanisms. Subsequently, we systematically progress to the fusion of information across different hierarchies. This progressive approach aims to capture nuanced details and global context, ensuring the comprehensive utilization of our hierarchical representation.

As shown in Fig. 1, PASTA sets new SOTA records on HDR benchmarks, validating its effectiveness and versatility. It also excels in efficiency, with fast inference speeds, low GPU memory usage, and reduced latency. Remarkably, PASTA outperforms existing SOTA methods in processing 1080P LDR images on a plain GPU with just 12GB of RAM, achieving a substantial 3-fold ($\times 3$) increase in inference speed. An ultra-lightweight version further enhances this, boosting speed by nearly 9 times ($\times 9$) while still maintaining a competitive level of performance.

2 Related Work

Rejection-based methods. These methods aim to identify and reject moving regions inconsistent with a reference frame’s background during synthesis. Various techniques, such as non-parametric estimation [22], local entropy [18], threshold bitmap [32, 40], intensity histogram [36], and bi-directional similarity [25, 68], detect moving pixels. However, they often lose fine details in dynamic

areas and struggle to adapt to different cameras and exposure settings due to fixed threshold reliance [12].

Registration-based methods. The emphasis is very much on aligning exposure images. In the case of only camera motion between exposure sources, *i.e.*, the captured scene is rigid and on a plane, simple operations such as translation [56], homography [51], correlation matching [1], and phase cross correlation [62] can be used to crack this challenge. For dynamic scenes, most methods seek non-grid dense correspondences (*e.g.*, joint homography and SIFT [14], joint homography and optical flow [21], and RANSAC [11, 16]) between images. However, the warped images are prone to holes in the presence of large displacements or severe occlusion.

Optimization-based methods. They jointly perform alignment and reconstruction in the form of an energy function, or only use the framework to perform one of them, for example, using Poisson equation [8, 10], graph cut [7], Markov random field [12, 19], Bayesian [32], energy-based optic flow [69], Patch-Match [17, 47], rank minimization [23, 39] and background estimation [13]. Despite progress, they fall short of learning-based methods in deghosting results and tend to be time-consuming.

Learning-based methods. They have evolved since [20], which uses optical flow [27] for image alignment in HDR creation. Subsequent works directly cascaded features [38, 57, 63] or utilize attention mechanisms [3, 24, 35, 59, 67] for implicit motion alignment, bypassing traditional optical flow techniques. Additionally, some methods integrate optical flow networks [2] or deformable convolutions [30] for spatial feature alignment. Non-local attention [60] and recurrent networks [41] have been used for large-scale motion modeling. Along with distinctive merits of Transformer [53], *i.e.*, long-range dependencies, which is particularly suitable for capturing large object displacement, recent deghosting approaches based on Transformers [28, 31, 48, 50, 58, 61] leverage the traits for large object displacement, with CA-ViT [31] and SCTNet [50] as new baselines using Swin Transformer block [29]. However, these methods face challenges: 1) losing Swin Transformer’s significantly hierarchical advantage; 2) visible block artifacts in tone-mapped results—the resulting to partition input images into blocks (*e.g.*, 256×256) for inference, as 2K images cannot be processed on limited-memory GPUs. The latest GDP [9] employs a pre-trained denoising diffusion probabilistic model (DDPM) [15] for image restoration, including HDR, but it’s limited by less realistic hole filling in occluded areas and slow inference speed.

3 Proposed Method

3.1 Preliminaries

Let $\{I_i\}_{i=1}^n$ be a set of LDR images with varying exposure times $\{t_i\}_{i=1}^n$. If the input is not in RAW format, they are transformed into the HDR domain via gamma correction, defined by the power-law expansion:

$$H_i = I_i^\gamma / t_i, \quad (1)$$

where I_i is raised to a gamma value $\gamma > 1$ and divided by time t_i to get the corresponding image H_i . In the common case of $\gamma = 2.2$, inputs and outputs are

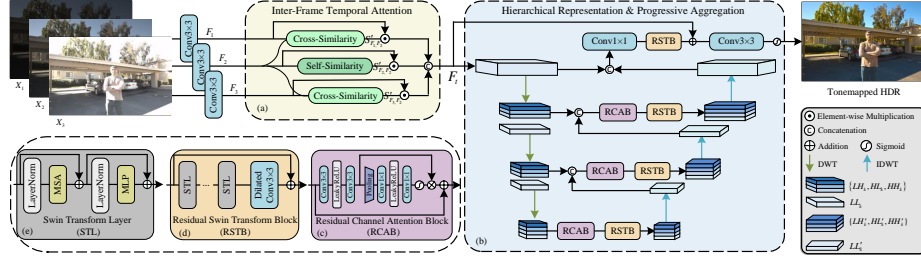


Fig. 2: Framework Overview. The proposed framework mainly consists of three stages, *i.e.*, shallow feature extraction, inter-frame temporal attention, and hierarchical representation & progressive aggregation.

typically normalized to the interval $[0, 1]$. Similar to previous works [20, 57], we take $\{X_i\}_{i=1}^n$ as the input, where $X_i = [I_i, H_i]$ concatenates I_i and H_i along the channel dimension. The acquisition of HDR imaging, H , is to find a mapping function φ with respect to the parameter θ , satisfying:

$$H = \varphi(X_1, X_2, \dots, X_n; \theta). \quad (2)$$

In this work, we also set $n = 3$ and use X_2 with a medium exposure as the reference frame, so that the motion content in the resulting HDR image H is consistent with it.

3.2 Overall Pipeline

Given a set of LDRs $\{X_i\}_{i=1}^3$, we utilize three separate 3×3 convolutions to extract corresponding shallow features $F_i \in \mathbb{R}^{H \times W \times C}$, where $X_i \in \mathbb{R}^{H \times W \times 6}$, $H \times W$ denotes the resolution of the image, and C denotes the number of channels. The architecture of PASTA, as depicted in Fig. 2, comprises two key components, *i.e.*, Inter-Frame Temporal Attention and Hierarchical Representation & Progressive Aggregation.

3.3 Inter-Frame Temporal Attention

The exposure stack captures the temporal information across frames. Previous works [31, 59] utilize spatial attention between reference and non-reference frames to suppress motion and saturation. Different from them, we replace spatial attention with temporal attention [55] because 1) different regions across frames are not equally informative due to exposure variations, occlusions, and moving objects. 2) The spatial attention is implemented by cascading the reference and non-reference frames instead of directly calculating their similarity, and then performing convolution with sigmoid activation to obtain the attention map. In fact, this computation way does not easily discern the differences between frames when both motion and saturation coexist [58]. 3) The computation of spatial attention can be regarded as a local form of self-attention mechanism.

IFTA module is illustrated in Fig. 2(a) with the aim of computing attention features between adjacent frames in the embedding space. For shallow feature $F_i \in \mathbb{R}^{H \times W \times C}$, $i \in \{1, 2, 3\}$, the similarity matrix $S \in \mathbb{R}^{H \times W}$ is obtained by:

$$S_{F_i, F_2}(x, y) = \langle \phi_i(x, y), \phi_2(x, y) \rangle, \quad (3)$$

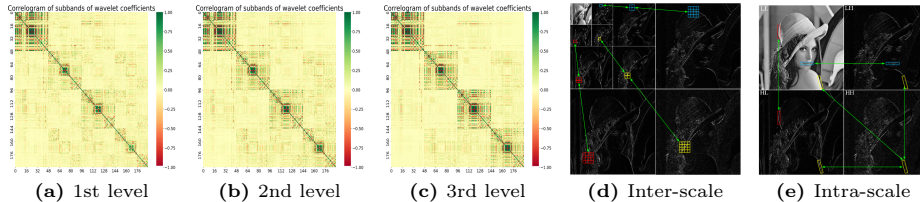


Fig. 3: (a)-(c) Feature Channels Correlation between subband coefficients of three levels of wavelet decomposition measured by Pearson correlation coefficient (PCCs). The channel dimension of each subband coefficient is 48. In each subfigure, from the top left to the bottom right, the correlations among the channels of the subband coefficients $\{LL_k, LH_k, HL_k, HH_k\}_{k=1}^3$ themselves are shown. **(d)-(e) Dependencies between wavelet coefficients** across different scales give rise to a quad-tree structure, where not only the parents but also the children coefficients contain pertinent information.

where x and y are feature coordinates, ϕ_i and ϕ_2 are two embeddings of corresponding features F_i and F_2 , achieved via a convolution operation, and $\langle \cdot, \cdot \rangle$ denotes the element-wise inner product along the channel dimension. After sigmoid function and channel expansion operations, we can obtain the attention map $S'_{F_i, F_2} \in \mathbb{R}^{H \times W \times C}$. The contribution of the sigmoid function lies in: i) *highlighting* misaligned and saturated feature regions; ii) By limiting the inner product output to $[0, 1]$, the function *keeps gradients in check* during backpropagation, enhancing *training stability*; iii) improving *convergence efficiency*. The similarity in the Eq. (3) belongs to an element-wise local attention mechanism. It is noted that Eq. (3) not only includes cross-similarity but also self-similarity for reference feature. This differs from spatial attention-based methods [31, 59] which indiscriminately concatenate the reference feature directly into the attention features. Then, temporal attention features $\{F_{i,t}\}_{i=1}^3$ can be obtained by element-wise multiplication of F_i and S_{F_i, F_2} , defined as $F_{i,t} = F_i \odot S'_{F_i, F_2}$.

Lastly, the temporal attention features mentioned above are concatenated by $F_t = \text{Cat}(F_{1,t}, F_{2,t}, F_{3,t})$.

3.4 Hierarchical Representation & Progressive Aggregation

To reduce the computational complexity of self-attention module, many works utilize pooling [54], patch merging [29], and pixel-shuffle [65] for down-sampling feature maps. These operations nevertheless are either irreversible [29, 54], which potentially lead to a drop in the capability of feature representation, especially for low-level pixel-wise visual tasks, or still suffer from excessive memory in case of high-resolution images due to the symmetric U-Net architecture [65]. Among of them, Swin [29] has demonstrated that hierarchy is of vital importance in vision tasks. In addition to the parallel computation achieved by shift window, the superiority of Swin over ViT [6] is mainly attributed to this paramount trait. However, existing Transformer-based dehazing works [28, 31, 58, 61], as well as SwinIR [26] represented by the use of Swin blocks, overlook or do not fully inherit the character of hierarchical representation.

The attractive properties of the wavelet transform enable it to well represent and decouple features, including *locality*, *multi-resolution*, *compression*, *clustering* and *persistence* [4, 46]. Figs. 3d and 3e show the magnitude values of wavelet coefficients at three scales and indicate that subbands are not statistically independent from visual inspection. Due to the non-Gaussianity of wavelet marginals, previous works have primarily utilized hidden Markov models [4, 46] to characterize the statistical dependencies between those coefficients. In this work, our objective is to develop a module to implicitly explore the relationships among subbands, which is rich and flexible enough to represent coefficient characteristics yet concise, tractable and efficient for high-resolution images.

Wavelet Representation. DWT, as a classic technique for multi-resolution, decomposes a 2D image into four subband components: one low-frequency band, LL , and three high-frequency ones, *i.e.*, LH , HL , and HH , with half the resolution of the source. The DWT is reversible, and its inverse, denoted as IDWT. As shown in Fig. 2(b), let $LL_0 = F_t$ and we recursively perform the DWT on the low-frequency component $\{LL_k\}_{k=0}^{K-1}$ at each scale k , obtaining a set of a set of high-frequency residual components $\{LH_k, HL_k, HH_k\}_{k=1}^K$ and the coarsest low-frequency approximated one LL_K . The low-frequency features identify the motion between frames, illumination variations, and color information, while the high-frequency ones capture contour information and rapid changes in appearance. As the decomposition level k increases, the resolution of the corresponding high- and low-frequency components decreases from $H \times W$ to $\frac{H}{2^k} \times \frac{W}{2^k}$ while keeping the channel dimension unchanged. Compared to the U-Net architecture of Restormer [65], our representation structure has no additional learnable parameters except for the fixed ones of the wavelet filters in terms of hierarchical representation. Furthermore, the channel dimension of Restormer doubles as the decomposition levels increase.

Coarse-to-Fine Aggregation. The wavelet representation not only expands the receptive field for the aggregation stage, which will foster ghost removal for large object displacement and large-disparity alignment, but also achieves feature decoupling, specifically for low- and high-frequency components. Recalling the remarkable properties of wavelet coefficients and the dependency on subband coefficients stated in Sec. 3.4, this inspires us to implicitly explore and utilize the statistical relationship. Figs. 3a to 3c illustrates the correlation coefficients between different frequency subband channels measured by PCCs. Correlation and redundancy among wavelet subband channels are evident. As the levels of DWT decomposition increase, the inter-channel correlation gradually intensifies.

As shown in Fig. 2(b), after three levels of DWT, we obtain the final low-frequency subband LL_3 and the corresponding detail ones $\{LH_3, HL_3, HH_3\}$. Taking into account the correlation between different frequency bands and the redundancy of subband features, we process them by concatenating the high and low-frequency subbands after wavelet decomposition. Another purpose of joint processing is to prevent the loss of spatial coherence between low and high frequencies when they are processed separately. It is common for the low frequencies

to remove ghosting, but the high frequencies fail to handle the boundaries or contours of moving objects effectively, thereby resulting in ghosting. The developed progressive aggregation strategy for large-scale dynamic scenes mainly includes four stages. The core module is composed of a residual channel attention block (RCAB) [66] and a residual Swin Transformer block (RSTB) [26], where RCAB is used to explore inter-subband dependencies, followed by RSTB to build long-range spatial dependencies. The first three stages involve aggregating within the space of wavelet representation with spatial contextual information. From bottom to top, *i.e.*, from global to local, our progressive aggregation framework iteratively upscales and refines the estimates from the previous level by predicting the high- and low-frequency coefficients. The last stage operates in the original feature space (without downsampling operations), thereby preserving fine details in the final reconstructed HDR image. Specifically, the reconstructed features LL'_0 are concatenated with the original features F_t . Then a 1×1 convolution is used to achieve channel dimension compression, followed by passing through an RSTB module.

Skip Connection. To construct a ghost-free HDR image, we have developed a model with a long skip connection extending from the IFTA feature F_t . This connection refines spatio-temporal aggregated features by merging the reconstructed wavelet coefficient features from the initial three stages with the finest features of the last stage. We have named this model **PASTA-I**, highlighting its capability for implicit alignment, which significantly reduces motion blur and ghosting effects in case of shooting moving scenes.

w and w/o IFTA Module. As the proposed model **PASTA-I** without IFTA strategy will simplify to cascading shallow features directly, akin to [38, 57], this subsection emphasizes the comparison of the developed variant with them. As we previously discussed, 1) Both methods [38, 57] are vulnerable to the cases with occlusions and large moving objects. 2) Self-attention inherently possesses alignment capabilities to some extent. In contrast, applying the self-attention mechanism to [38, 57], *i.e.*, our alignment-free variant **PASTA-U**, is competent to handle these scenarios. To circumvent the generation of ghosting artifacts, **PASTA-I**'s long skip F_t is replaced in **PASTA-U** with $\text{Conv}_{3 \times 3}(F_2)$, which considers the motion in intermediate frames to direct network learning. The results from **PASTA-U** show that: i) Self-attention can directly leverage unaligned feature information, and ii) A hierarchical structure can facilitate the enhancement of the self-attention mechanism's ability to utilize unaligned feature information. This is actually evidenced by the fact that Swin [29] outperforms ViT [6].

3.5 Loss Function

We use μ -law function to map the HDR image from the linear domain to the tonemapped domain through $\mathcal{T}(x) = \frac{\log(1+\mu x)}{\log(1+\mu)}$,

where $\mathcal{T}(\cdot)$ is the tone mapping function, $\mu = 5000$. In the tonemapped domain, in addition to the previous loss functions [31, 58] that consist of \mathcal{L}_1 loss and perceptual loss \mathcal{L}_p , we further incorporate a edge loss \mathcal{L}_e to surpass the edge blurring possibly caused by the hierarchical representation, which is defined as:

$$\mathcal{L}_e = \sqrt{\left\| \nabla(\mathcal{T}(H)) - \nabla(\mathcal{T}(\hat{H})) \right\|^2 + \varepsilon^2}, \quad (4)$$

where \hat{H} is the estimated HDR image, and the constant ε is empirically set to 10^{-3} .

Overall, our loss function is $\mathcal{L} = \mathcal{L}_1 + \alpha\mathcal{L}_p + \beta\mathcal{L}_e$, where α and β are set to 0.01 and 1, respectively.

4 Experiments

4.1 Experimental Settings

Datasets. We train the proposed model on Kalantari *et al.*’s [20] and Tel *et al.*’s [50] datasets, which consist of 74/15 training/testing scenes and 108/36 counterparts, respectively.

We first crop the images in the training set into image patches of size 128×128 with a stride of 64, and then perform a clockwise rotation of 90° , and horizontal and vertical flips for data augmentation. To validate the effectiveness of the proposed method, we also conduct testing on Sen *et al.*’s [47] and Tursen *et al.*’s [52] datasets.

Metrics. We use five commonly used metrics, *i.e.*, PSNR- l , PSNR- μ , SSIM- l , SSIM- μ , and HDR-VDP-2 [34], to evaluate the performance of different methods. Here, ‘ l ’ and ‘ μ ’ refer to the calculation of the respective metrics in the linear and tonemapped domain, respectively. HDR-VDP-2 is a visual metric tailored for HDR and its two parameters are set to 25 and 0.5, respectively, for the Kalantari *et al.*’s dataset. To ensure a fair comparison, we follow the same parameter settings [50] on Tel *et al.*’s dataset.

Implementation Details. Our model is implemented based on PyTorch and uses the Adam optimizer with an initial learning rate of $2e-4$, where β_1 , β_2 , and ε are set to 0.9, 0.999, and $1e-8$, respectively. The total number of iterations is 300K, and the learning rate is halved every 50K ones. We set the batch size to 16 and trained on 8 NVIDIA TITAN Xp GPUs. Tab. 2 lists the parameter configurations, highlighting the tiny version’s key differences in channel dimension, Swin Transformer layers (STL), and multi-head self-attention heads.

Table 2: Model architecture configuration. “ C ”, “Reduction” and “Win. sz.” refer to the channel dimension in shallow feature F_i , the channel reduction factor for each RCAB, and the window size in the RSTB, respectively.

Model	C	Num. of STL	Num. of heads	Reduction	MLP ratio	Win. sz.	#Param.
PASTA-I	16	[6, 6, 6, 6]	[4, 4, 4, 4]	[4, 4, 4]	2	8	8.163M
PASTA-I-Tiny	12	[2, 2, 2, 2]	[3, 3, 3, 3]	[4, 4, 4]	2	8	2.636M
PASTA-U	16	[6, 6, 6, 6]	[4, 4, 4, 4]	[4, 4, 4]	2	8	8.165M
PASTA-U-Tiny	12	[2, 2, 2, 2]	[3, 3, 3, 3]	[4, 4, 4]	2	8	2.637M

4.2 Comparison with SOTAs

We evaluate PASTA against 16 SOTA methods that include Sen *et al.* [47], Hu *et al.* [17], Kalantari *et al.* [20], DeepHDR [57], AHDRNet [59], PAMNet [44],

Table 3: Quantitative comparison with state-of-the-art methods on Kalantari *et al.*'s [20] and Tel *et al.*'s [50] datasets. “-” indicates that the code or pretrained weight is not available, and the parameters for calculating HDR-VDP-2 (H.V.-2) are unspecified. The top two performers under each metric are highlighted in red and blue, respectively.

Dataset	Method	Venue	H.V.-2 \uparrow	Linear Imgs.		Tonemapped Imgs.		
				PSNR- l \uparrow	SSIM- l \uparrow	PSNR- μ \uparrow	SSIM- μ \uparrow	
Kalantari	Sen <i>et al.</i> [47]	TOG'12	59.38	38.11	0.9721	40.80	0.9808	
	Hu <i>et al.</i> [17]	CVPR'13	-	30.76	0.9503	35.79	0.9717	
	Kalantari <i>et al.</i> [20]	TOG'17	64.18	41.23	0.9846	42.67	0.9888	
	DeepHDR [57]	ECCV'18	64.90	40.88	0.9858	41.65	0.9860	
	AHDRNet [59]	CVPR'19	65.61	41.14	0.9702	43.63	0.9900	
	PAMNet [44]	ACCV'20	-	41.65	0.9870	43.85	0.9906	
	NHDRRnet [60]	TIP'20	64.08	41.08	0.9861	42.41	0.9887	
	PSFNet [63]	MM'21	-	41.57	0.9867	44.06	0.9907	
	HDRRNN [41]	TIP'21	-	41.68	-	42.07	-	
	HDR-GAN [38]	TIP'21	65.54	41.57	0.9865	43.92	0.9905	
	APNT [3]	TIP'22	-	41.61	0.9879	43.94	0.9898	
	FHDRNet [5]	CVIU'24	65.71	41.47	0.9869	43.91	0.9908	
	STHDR [48]	ECCV'22	-	41.70	0.9872	44.10	0.9909	
	CA-ViT [31]	ECCV'22	65.66	42.18	0.9884	44.32	0.9916	
	SCTNet [50]	ICCV'23	64.48	42.29	0.9887	44.49	0.9924	
	PASTA-I	Ours		65.92	42.50	0.9899	44.53	0.9918
PASTA-U	Ours		65.86	42.45	0.9895	44.49	0.9917	
Tel	Kalantari <i>et al.</i> [20]	TOG'17	67.09	43.37	0.9924	40.05	0.9794	
	NHDRRnet [60]	TIP'20	65.41	39.61	0.9853	36.68	0.9590	
	AHDRNet [59]	CVPR'19	68.80	45.30	0.9943	42.08	0.9837	
	FHDRNet [5]	CVIU'24	69.86	45.80	0.9948	42.41	0.9858	
	CA-ViT [31]	ECCV'22	69.23	46.35	0.9948	42.39	0.9844	
	SCTNet [50]	ICCV'23	70.66	47.51	0.9952	42.55	0.9850	
	PASTA-I	Ours		71.30	48.24	0.9961	43.53	0.9883
	PASTA-U	Ours		71.20	48.16	0.9961	43.62	0.9884

NHDRRnet [60], PSFNet [63], FSHDR [43], HDRRNN [41], HDR-GAN [38], APNT [3], FHDRNet [5], STHDR [48], CA-ViT [31], and SCTNet [50].

Quantitative Comparison. Tab. 3 shows that PASTA-I and PASTA-U perform competitively on two benchmarks, excelling particularly on the latest [50]. Notably, both models significantly outperform the latest baseline, CA-ViT, by margins of 0.32dB/0.26dB and 0.21dB/0.17dB in PSNR- l /PSNR- μ on Kalantari *et al.*'s dataset. Additionally, we have observed that HDR-VDP-2 metrics do not consistently exhibit proportionality to PSNR values. On Tel *et al.*'s dataset, our methods surpass top contenders like SCTNet and CA-ViT across all metrics. PASTA-U's performance suggests that self-attention allows for effective ghost-free HDR image reconstruction even with some large misalignment. It should be noted that some of the values in Tab. 3 are derived from [31, 50, 58].

Qualitative Comparison. Figs. 4 and 5 show two challenging scenes: large-scale foreground motion and significant camera motion with large disparities. The coexistence of occlusions and saturation is inevitable and intractable in the presence of exposure and motion variations. In such case, non-attention or non-transformer-based methods like the approaches of Sen *et al.* and Kalantari *et al.*, DeepHDR, NHDRRnet, HDRRNN and FSHDR struggle with ghosting artifacts due to unreliable alignment (*e.g.*, optical flow, homography) or lack of



Fig. 4: Visual comparison of large-scale foreground and dense background motion with SOTA methods on Kalantari *et al.*'s dataset [20].

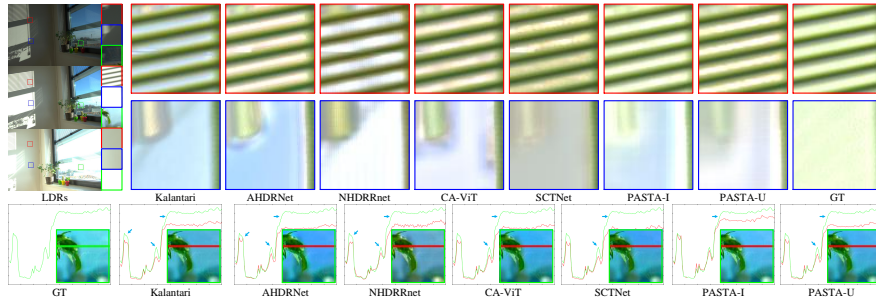


Fig. 5: Visual comparison of large disparities with SOTA methods on Tel *et al.*'s dataset [50]. The bottom row displays 1D intensity shift of the green close-up regions labeled with the line. Zoom in for better viewing.

feature alignment, often failing in fine detail preservation, such as hair in Fig. 4. Additionally, the patch-based method of Sen *et al.* incurs noticeable halos. In contrast, our method surpasses others like CA-ViT, SCT-Net and AHDRNet in ghosting removal, saturation handling, detail retention, and color consistency. In window scenes with significant disparities, approaches like Kalantari *et al.* and NHDRNet suffer content loss in saturated areas, while CA-ViT and SCTNet struggle with fine detail recovery and noise suppression, as shown in Fig. 5's red close-up regions. By comparison, our method achieves relatively noise-free results in these areas. The proposed method, especially PASTA-I, also preserve edge sharpness and intensity in smooth regions better than competitors like CA-ViT and SCTNet, evident in the green close-ups in Fig. 5. For additional results, please refer to the supplementary materials.

4.3 Ablation Study

Here, taking **PASTA-I** as an example, we validate our framework's efficacy via IFTA, RCAB, edge loss, among others, as detailed in Tabs. 4 and 5.

Effectiveness of IFTA. To validate the effectiveness of IFTA, we replaced it with spatial attention [31,59], *i.e.*, SA vs. IFTA, and directly removed it, *i.e.*, w/o IFTA, respectively. The performance of the variant based on spatial attention is slightly lower than w/o IFTA and our full model, especially in terms of PSNR- l by a margin of 0.47dB and 0.64dB, respectively. As we mentioned in Sec. 3.3,

Table 4: Ablation study including IFTA, RCAB, \mathcal{L}_p and \mathcal{L}_e on the Kalantari *et al.* ’ dataset [20] using PASTA-I (Ours). “SA vs. IFTA” refers to IFTA being replaced with spatial attention.

Metrics	SA vs. IFTA	w/o IFTA	w/o RCAB	w/o \mathcal{L}_p	w/o \mathcal{L}_e	PASTA-U	PASTA-I
PSNR- l	41.86	42.33	42.19	42.61	42.45	42.45	42.50
SSIM- l	0.9897	0.9896	0.9895	0.9897	0.9893	0.9895	0.9899
PSNR- μ	44.40	44.45	43.96	44.46	44.40	44.49	44.53
SSIM- μ	0.9918	0.9916	0.9917	0.9919	0.9917	0.9917	0.9918

Table 5: Ablation studies of sampling methods and DWT scales. “PUS vs DWT” indicates using PixelUnshuffle (PUS) [65] to replace DWT for downsampling, and Pixelshuffle to replace IDWT for upsampling. “Conv. vs DWT” denotes the substitution of the DWT with convolution, as used in [5, 57, 60]. “ K ” is the scale of the hierarchical representation structure.

Settings	Variant	Kalantari <i>et al.</i> ’s [20]		1000×1500		2560×1440	
		#Imgs- l	#Imgs- μ	G. Mem.	Time	G. Mem.	Time
Sampling methods	PUS vs. DWT	37.19/.9775	40.23/.9852	7.729	2.353	OOM	-
	Conv. vs. DWT	42.07/.9880	44.52/.9916	7.725	2.516	18.399	5.871
DWT scales	PASTA-I ($K=1$)	42.20/.9887	44.46/.9917	7.298	2.382	17.464	5.520
	PASTA-I ($K=2$)	42.39/.9893	44.42/.9917	7.629	2.511	17.968	5.639
	PASTA-I ($K=4$)	42.31/.9895	44.35/.9916	7.869	2.550	19.584	5.942
Our plain version with $K=3$	PASTA-I	42.50/.9899	44.53/.9918	7.850	2.543	18.743	5.891
	PASTA-I-Tiny	42.25/.9890	44.46/.9917	6.015	0.829	14.399	1.889

i) The indiscriminate concatenation of reference frame features into attention features by spatial attention may degrade the network performance in case of occlusions and saturation coexisting in the reference frames; ii) The computation of spatial attention can be seen as a localized form of self-attention mechanism, which also indicates that self-attention has a certain alignment effect.

Effectiveness of RCAB. The RCAB module is integral to our framework, focusing on the dependencies both within and across scales of wavelet subband coefficients. When RCAB is removed, we observe a significant reduction in both PSNR- l and PSNR- μ by 0.31dB and 0.57dB. This indicates that the superiority of our framework lies in its implicit statistical modeling of wavelet coefficients.

Effectiveness of Edge Loss. The variant w/o \mathcal{L}_p , *i.e.*, only \mathcal{L}_1 and \mathcal{L}_e , achieved a higher PSNR- l of 42.61dB, suggesting that this loss prevents edge blurring during the process of progressive aggregation, thereby reducing or avoiding halo artifacts. Additionally, its SSIM- μ slightly improved to 0.9919, indicating a potential trade-off between the objective quality of exposure and the perceived quality of texture and structure. The variant, w/o \mathcal{L}_e , falls slightly behind in all metrics compared to the variant w/o \mathcal{L}_p . Our full model indicates that \mathcal{L}_e plays a subtle yet tangible role in reconstructing high-frequency detail, while edge loss in preserving edge sharpness.

Sampling methods and DWT scales. We also replace the DWT operation with alternative sampling methods. The results, listed in the upper section of Tab. 5, affirm our efficacy. In comparison with Conv-based methods, our PASTA-I-tiny achieved a +0.18dB improvement with only 77% memory utilization, simultaneously accelerating inference time by a factor of $\times 3$.

Table 6: Comparison of GPU memory (G) consumption and average inference time (seconds) for three LDR images with different resolutions, *i.e.*, 1000×1500 and 2560×1440 (2K), implements on a RTX 3090 GPU (24G). OOM and ‘-’ refer to the out-of-memory and being unavailable, respectively.

Method	Tel <i>et al.</i> 's [50]		Kalantari <i>et al.</i> 's [20]		1000×1500		2560×1440	
	#Imgs- l	#Imgs- μ	#Imgs- l	#Imgs- μ	G. Mem.	Time	G. Mem.	Time
AHDRNet [59] (CVPR'19)	45.30/.9943	42.08/.9837	41.14/.9702	43.63/.9900	9.069	0.348	OOM	-
FHDRNet [5] (CVIU'24)	45.80/.9948	42.41/.9858	41.47/.9869	43.91/.9908	5.643	0.329	13.449	0.985
CA-ViT [31] (ECCV'22)	46.35/.9948	42.39/.9844	42.18/.9884	44.32/.9916	10.637	4.631	OOM	-
SCTNet [50] (ICCV'23)	47.51/.9952	42.55/.9850	42.29/.9887	44.49/.9924	9.732	6.621	OOM	-
PASTA-I	48.24/.9961	43.53/.9883	42.50/.9899	44.53/.9918	7.850	2.418	18.743	5.969
PASTA-I-Tiny	48.08/.9957	43.45/.9878	42.25/.9890	44.46/.9917	6.015	0.867	14.399	2.071
PASTA-U	48.16/.9961	43.62/.9884	42.45/.9895	44.49/.9917	7.850	2.242	18.743	5.765
PASTA-U-Tiny	48.08/.9960	43.51/.9879	42.07/.9883	44.43/.9916	6.015	0.773	14.402	2.036

4.4 Efficiency Analysis

Wavelet Representation. Efficiency is achieved through the use of DWT for feature extraction. DWT requires no additional learned parameters and isotropic feature extraction avoids increasing channel capacity. It efficiently captures multi-scale information.

Progressive Hierarchical Aggregation. Our progressive hierarchical aggregation strategy speeds up the network by processing lower-resolution representations and iteratively refining them. This approach efficiently retains essential information while discarding redundant details.

Quantitative Results. Tab. 6 reports GPU memory consumption (G. Mem.)⁵ and average inference time of our methods and four baselines on three LDR inputs of different resolutions, calculated over 100 iterations. Taking the resolution of 1000×1500 as an example, benefiting from the hierarchical representation and progressive aggregation, the proposed method achieves GPU costs of 74% compared to CA-ViT and 80% to SCTNet; the inference speed is nearly 2.8 times faster than SCTNet, 2 times than CA-ViT. When inputs are 2K, aside from the FHDRNet, none of the aforementioned baselines can directly perform inference. Tabs. 3 and 6 indicate that the proposed method achieves the best balance in inference time, GPU memory usage and reconstruction performance compared to SOTA methods, especially those [31, 50, 58] utilizing Transformer.

4.5 Discussion

Occlusion Coexist with Saturation. In both our method and CA-ViT [31], pixel recovery encounters hurdles when occlusions coincide with saturation, as depicted in Fig. 6, mirroring challenges observed in human perception. Despite these obstacles, our model outperforms CA-ViT, generating more realistic estimates. In fact, the effective generation of high-fidelity HDR images without ghosting benefits from neighboring frames compensating for occlusions, illustrated in the pink and red regions. Complications typically arise when the corresponding region in neighboring frames is saturated, hindering realistic content hallucination, as seen in the blue and green areas. While techniques like diffusion models [9, 15] or inpainting may be applied, they may not produce realistic results. For such case, leveraging occlusion rather than attempting to hallucinate

⁵ Computed by PyTorch `torch.cuda.max_memory_allocated()` function.

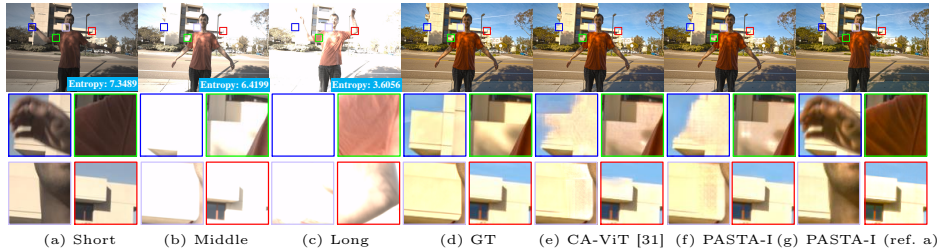


Fig. 6: Two types of occlusion, *i.e.*, compensatory and non-compensatory occlusion (NCO). The former denotes the provision of beneficial information in the corresponding regions between frames, *e.g.*, the enlarged red region, while the latter the simultaneous presence of occlusion and saturation in the corresponding regions between frames *e.g.*, the first three close-up regions. NCO can be effectively utilized by re-selecting the reference frame from the perspective of maximizing information (*e.g.*, entropy), rather than attempting to hallucinate or fill in the occluded regions. Among them, “PASTA-I (ref. a)” is generated using the proposed method, where “short” is selected as the *reference frame* with entropy-maximization in the exposure sequence. This strategy ensures a high-fidelity result without ghosting.

could be a practical approach. Opting for a frame with maximum information content (*e.g.*, entropy) as the reference from the exposure sequence can be advantageous. Success with image entropy in measuring pixel uncertainty [18] supports this strategy. When constructing datasets or developing unsupervised models, prioritizing frames with maximum information content as references may alleviate occlusion effects.

Potential Drawback to Benchmarks. Despite some SOTA methods achieving high PSNR- l values on benchmarks [20, 28, 50], significant deviations to around 30dB are observed in certain test cases. This discrepancy is attributed to non-compensatory occlusions and dense subtle motion, challenging pixel-wise evaluation metrics. Wind-induced subtle motion during outdoor shooting, impacting scenes like tree branches, leaves, grass, clouds, and flowing water, can have a substantial effect. This requires a further in-depth reflection on the GT generation approach.

5 Conclusions

This work proposes a flexible and efficient framework, PASTA, to address HDR deghosting’s computational challenges, which optimizes the trade-off between performance and computational efficiency, particularly at high resolutions. By integrating hierarchical feature decoupling and progressive aggregation, PASTA significantly boosts inference speed, achieving a significant threefold improvement, and can even reach a ninefold increase without sacrificing image quality. The comprehensive experiments validate that PASTA not only rivals but surpasses the existing SOTA methods in performance metrics, all while streamlining the use of computational resources.

References

1. Akyüz, A.O.: Photographically guided alignment for hdr images. In: Eurographics (Areas Papers). pp. 73–74 (2011)
2. Catley-Chandar, S., Tanay, T., Vandroux, L., Leonardis, A., Slabaugh, G., Pérez-Pellitero, E.: Flexhdr: Modeling alignment and exposure uncertainties for flexible hdr imaging. *IEEE Transactions on Image Processing* **31**, 5923–5935 (2022)
3. Chen, J., Yang, Z., Chan, T.N., Li, H., Hou, J., Chau, L.P.: Attention-guided progressive neural texture fusion for high dynamic range image restoration. *IEEE Transactions on Image Processing* **31**, 2661–2672 (2022)
4. Crouse, M.S., Nowak, R.D., Baraniuk, R.G.: Wavelet-based statistical signal processing using hidden markov models. *IEEE Transactions on signal processing* **46**(4), 886–902 (1998)
5. Dai, T., Li, W., Cao, X., Liu, J., Jia, X., Leonardis, A., Yan, Y., Yuan, S.: Wavelet-based network for high dynamic range imaging. *Computer Vision and Image Understanding* **238**, 103881 (2024)
6. Dosovitskiy, A., Beyer, L., Kolesnikov, A., Weissenborn, D., Zhai, X., Unterthiner, T., Dehghani, M., Minderer, M., Heigold, G., Gelly, S., et al.: An image is worth 16x16 words: Transformers for image recognition at scale. *ICLR* (2021)
7. Eden, A., Uyttendaele, M., Szeliski, R.: Seamless image stitching of scenes with large motions and exposure differences. In: *IEEE Conference on Computer Vision and Pattern Recognition*. vol. 2, pp. 2498–2505. IEEE (2006)
8. Fattal, R., Lischinski, D., Werman, M.: Gradient domain high dynamic range compression. In: *Proceedings of the 29th annual conference on Computer graphics and interactive techniques*. pp. 249–256 (2002)
9. Fei, B., Lyu, Z., Pan, L., Zhang, J., Yang, W., Luo, T., Zhang, B., Dai, B.: Generative diffusion prior for unified image restoration and enhancement. In: *Proceedings of the IEEE/CVF Conference on Computer Vision and Pattern Recognition*. pp. 9935–9946 (2023)
10. Gallo, O., Gelfandz, N., Chen, W.C., Tico, M., Pulli, K.: Artifact-free high dynamic range imaging. In: *IEEE International conference on computational photography*. pp. 1–7. IEEE (2009)
11. Gallo, O., Troccoli, A., Hu, J., Pulli, K., Kautz, J.: Locally non-rigid registration for mobile hdr photography. In: *Proceedings of the IEEE conference on computer vision and pattern recognition Workshops*. pp. 49–56 (2015)
12. Granados, M., Kim, K.I., Tompkin, J., Theobalt, C.: Automatic noise modeling for ghost-free hdr reconstruction. *ACM Transactions on Graphics (TOG)* **32**(6), 1–10 (2013)
13. Granados, M., Seidel, H.P., Lensch, H.P.: Background estimation from non-time sequence images. In: *Proceedings of graphics interface 2008*. pp. 33–40 (2008)
14. Heo, Y.S., Lee, K.M., Lee, S.U., Moon, Y., Cha, J.: Ghost-free high dynamic range imaging. In: *Asian Conference on Computer Vision*. pp. 486–500. Springer (2010)
15. Ho, J., Jain, A., Abbeel, P.: Denoising diffusion probabilistic models. *Advances in neural information processing systems* **33**, 6840–6851 (2020)
16. Hu, J., Gallo, O., Pulli, K.: Exposure stacks of live scenes with hand-held cameras. In: *European Conference on Computer Vision*. pp. 499–512. Springer (2012)
17. Hu, J., Gallo, O., Pulli, K., Sun, X.: Hdr deghosting: How to deal with saturation? In: *Proceedings IEEE Conference on Computer Vision and Pattern Recognition*. pp. 1163–1170 (2013)

18. Jacobs, K., Loscos, C., Ward, G.: Automatic high-dynamic range image generation for dynamic scenes. *IEEE Computer Graphics and Applications* **28**(2), 84–93 (2008)
19. Jinno, T., Okuda, M.: Motion blur free hdr image acquisition using multiple exposures. In: *IEEE International Conference on Image Processing*. pp. 1304–1307. IEEE (2008)
20. Kalantari, N.K., Ramamoorthi, R., et al.: Deep high dynamic range imaging of dynamic scenes. *ACM Trans. Graph.* **36**(4), 144–1 (2017)
21. Kang, S.B., Uyttendaele, M., Winder, S., Szeliski, R.: High dynamic range video. *ACM Transactions on Graphics (TOG)* **22**(3), 319–325 (2003)
22. Khan, E.A., Akyuz, A.O., Reinhard, E.: Ghost removal in high dynamic range images. In: *2006 International Conference on Image Processing*. pp. 2005–2008. IEEE (2006)
23. Lee, C., Li, Y., Monga, V.: Ghost-free high dynamic range imaging via rank minimization. *IEEE signal processing letters* **21**(9), 1045–1049 (2014)
24. Li, F., Gang, R., Li, C., Li, J., Ma, S., Liu, C., Cao, Y.: Gamma-enhanced spatial attention network for efficient high dynamic range imaging. In: *Proceedings of the IEEE/CVF Conference on Computer Vision and Pattern Recognition*. pp. 1032–1040 (2022)
25. Li, Z., Zheng, J., Zhu, Z., Wu, S.: Selectively detail-enhanced fusion of differently exposed images with moving objects. *IEEE Transactions on Image Processing* **23**(10), 4372–4382 (2014)
26. Liang, J., Cao, J., Sun, G., Zhang, K., Van Gool, L., Timofte, R.: Swinir: Image restoration using swin transformer. In: *Proceedings of the IEEE/CVF international conference on computer vision*. pp. 1833–1844 (2021)
27. Liu, C., et al.: Beyond pixels: exploring new representations and applications for motion analysis. Ph.D. thesis, Massachusetts Institute of Technology (2009)
28. Liu, S., Zhang, X., Sun, L., Liang, Z., Zeng, H., Zhang, L.: Joint hdr denoising and fusion: A real-world mobile hdr image dataset. In: *Proceedings of the IEEE/CVF Conference on Computer Vision and Pattern Recognition*. pp. 13966–13975 (2023)
29. Liu, Z., Lin, Y., Cao, Y., Hu, H., Wei, Y., Zhang, Z., Lin, S., Guo, B.: Swin transformer: Hierarchical vision transformer using shifted windows. In: *Proceedings of the IEEE/CVF international conference on computer vision*. pp. 10012–10022 (2021)
30. Liu, Z., Lin, W., Li, X., Rao, Q., Jiang, T., Han, M., Fan, H., Sun, J., Liu, S.: Adnet: Attention-guided deformable convolutional network for high dynamic range imaging. In: *Proceedings of the IEEE/CVF Conference on Computer Vision and Pattern Recognition*. pp. 463–470 (2021)
31. Liu, Z., Wang, Y., Zeng, B., Liu, S.: Ghost-free high dynamic range imaging with context-aware transformer. In: *European Conference on Computer Vision*. pp. 344–360. Springer (2022)
32. Lu, P.Y., Huang, T.H., Wu, M.S., Cheng, Y.T., Chuang, Y.Y.: High dynamic range image reconstruction from hand-held cameras. In: *IEEE Conference on Computer Vision and Pattern Recognition*. pp. 509–516. IEEE (2009)
33. Mallat, S.G.: A theory for multiresolution signal decomposition: the wavelet representation. *IEEE transactions on pattern analysis and machine intelligence* **11**(7), 674–693 (1989)
34. Mantiuk, R., Kim, K.J., Rempel, A.G., Heidrich, W.: Hdr-vdp-2: A calibrated visual metric for visibility and quality predictions in all luminance conditions. *ACM Transactions on graphics (TOG)* **30**(4), 1–14 (2011)

35. Marín-Vega, J., Sloth, M., Schneider-Kamp, P., Röttger, R.: Drhdr: A dual branch residual network for multi-bracket high dynamic range imaging. In: Proceedings of the IEEE/CVF Conference on Computer Vision and Pattern Recognition. pp. 844–852 (2022)
36. Min, T.H., Park, R.H., Chang, S.: Histogram based ghost removal in high dynamic range images. In: IEEE International Conference on Multimedia and Expo. pp. 530–533. IEEE (2009)
37. Myszkowski, K., Mantiuk, R., Krawczyk, G.: High dynamic range video. Springer Nature (2022)
38. Niu, Y., Wu, J., Liu, W., Guo, W., Lau, R.W.: Hdr-gan: Hdr image reconstruction from multi-exposed ldr images with large motions. *IEEE Transactions on Image Processing* **30**, 3885–3896 (2021)
39. Oh, T.H., Lee, J.Y., Tai, Y.W., Kweon, I.S.: Robust high dynamic range imaging by rank minimization. *IEEE transactions on pattern analysis and machine intelligence* **37**(6), 1219–1232 (2014)
40. Pece, F., Kautz, J.: Bitmap movement detection: Hdr for dynamic scenes. In: 2010 Conference on Visual Media Production. pp. 1–8. IEEE (2010)
41. Prabhakar, K.R., Agrawal, S., Babu, R.V.: Self-gated memory recurrent network for efficient scalable hdr deghosting. *IEEE Transactions on Computational Imaging* **7**, 1228–1239 (2021)
42. Prabhakar, K.R., Agrawal, S., Singh, D.K., Ashwath, B., Babu, R.V.: Towards practical and efficient high-resolution hdr deghosting with cnn. In: European Conference on Computer Vision. pp. 497–513. Springer (2020)
43. Prabhakar, K.R., Senthil, G., Agrawal, S., Babu, R.V., Gorthi, R.K.S.S.: Labeled from unlabeled: Exploiting unlabeled data for few-shot deep hdr deghosting. In: Proceedings of the IEEE/CVF Conference on Computer Vision and Pattern Recognition. pp. 4875–4885 (2021)
44. Pu, Z., Guo, P., Asif, M.S., Ma, Z.: Robust high dynamic range (hdr) imaging with complex motion and parallax. In: Proceedings of the Asian Conference on Computer Vision (2020)
45. Ramamonjisoa, M., Firman, M., Watson, J., Lepetit, V., Turmukhambetov, D.: Single image depth prediction with wavelet decomposition. In: Proceedings of the IEEE/CVF conference on computer vision and pattern recognition. pp. 11089–11098 (2021)
46. Romberg, J.K., Choi, H., Baraniuk, R.G.: Bayesian tree-structured image modeling using wavelet-domain hidden markov models. *IEEE Transactions on image processing* **10**(7), 1056–1068 (2001)
47. Sen, P., Kalantari, N.K., Yaesoubi, M., Darabi, S., Goldman, D.B., Shechtman, E.: Robust patch-based hdr reconstruction of dynamic scenes. *ACM Trans. Graph.* **31**(6), 203–1 (2012)
48. Song, J.W., Park, Y.I., Kong, K., Kwak, J., Kang, S.J.: Selective transhdr: Transformer-based selective hdr imaging using ghost region mask. In: European Conference on Computer Vision. pp. 288–304. Springer (2022)
49. Tel, S., Heyrman, B., Ginhac, D.: Cen-hdr: Computationally efficient neural network for real-time high dynamic range imaging. In: European Conference on Computer Vision. pp. 378–394. Springer (2022)
50. Tel, S., Wu, Z., Zhang, Y., Heyrman, B., Demonceaux, C., Timofte, R., Ginhac, D.: Alignment-free hdr deghosting with semantics consistent transformer. arXiv preprint p. arXiv:2305.18135 (2023)

51. Tomaszewska, A., Mantiuk, R.: Image registration for multi-exposure high dynamic range image acquisition. In: International Conference in Central Europe on Computer Graphics. pp. 49–56 (2007)
52. Tursun, O.T., Akyüz, A.O., Erdem, A., Erdem, E.: The state of the art in hdr deghosting: A survey and evaluation. *Computer Graphics Forum* **34**(2), 683–707 (2015)
53. Vaswani, A., Shazeer, N., Parmar, N., Uszkoreit, J., Jones, L., Gomez, A.N., Kaiser, Ł., Polosukhin, I.: Attention is all you need. In: *Advances in neural information processing systems*. vol. 30 (2017)
54. Wang, W., Xie, E., Li, X., Fan, D.P., Song, K., Liang, D., Lu, T., Luo, P., Shao, L.: Pyramid vision transformer: A versatile backbone for dense prediction without convolutions. In: *Proceedings of the IEEE/CVF international conference on computer vision*. pp. 568–578 (2021)
55. Wang, X., Chan, K.C., Yu, K., Dong, C., Change Loy, C.: Edvr: Video restoration with enhanced deformable convolutional networks. In: *Proceedings of the IEEE/CVF conference on computer vision and pattern recognition workshops*. pp. 0–0 (2019)
56. Ward, G.: Fast, robust image registration for compositing high dynamic range photographs from hand-held exposures. *Journal of graphics tools* **8**(2), 17–30 (2003)
57. Wu, S., Xu, J., Tai, Y.W., Tang, C.K.: Deep high dynamic range imaging with large foreground motions. In: *Proceedings of the European Conference on Computer Vision (ECCV)*. pp. 117–132 (2018)
58. Yan, Q., Chen, W., Zhang, S., Zhu, Y., Sun, J., Zhang, Y.: A unified hdr imaging method with pixel and patch level. In: *Proceedings of the IEEE/CVF Conference on Computer Vision and Pattern Recognition*. pp. 22211–22220 (2023)
59. Yan, Q., Gong, D., Shi, Q., Hengel, A.v.d., Shen, C., Reid, I., Zhang, Y.: Attention-guided network for ghost-free high dynamic range imaging. In: *Proceedings of the IEEE/CVF Conference on Computer Vision and Pattern Recognition*. pp. 1751–1760 (2019)
60. Yan, Q., Zhang, L., Liu, Y., Zhu, Y., Sun, J., Shi, Q., Zhang, Y.: Deep hdr imaging via a non-local network. *IEEE Transactions on Image Processing* **29**, 4308–4322 (2020)
61. Yan, Q., Zhang, S., Chen, W., Tang, H., Zhu, Y., Sun, J., Van Gool, L., Zhang, Y.: Smae: Few-shot learning for hdr deghosting with saturation-aware masked autoencoders. In: *Proceedings of the IEEE/CVF Conference on Computer Vision and Pattern Recognition*. pp. 5775–5784 (2023)
62. Yao, S.: Robust image registration for multiple exposure high dynamic range image synthesis. In: *Image Processing: Algorithms and Systems IX*. vol. 7870, pp. 216–224. SPIE (2011)
63. Ye, Q., Xiao, J., Lam, K.m., Okatani, T.: Progressive and selective fusion network for high dynamic range imaging. In: *Proceedings of the 29th ACM International Conference on Multimedia*. pp. 5290–5297 (2021)
64. Yu, Y., Zhan, F., Lu, S., Pan, J., Ma, F., Xie, X., Miao, C.: Wavefill: A wavelet-based generation network for image inpainting. In: *Proceedings of the IEEE/CVF international conference on computer vision*. pp. 14114–14123 (2021)
65. Zamir, S.W., Arora, A., Khan, S., Hayat, M., Khan, F.S., Yang, M.H.: Restormer: Efficient transformer for high-resolution image restoration. In: *Proceedings of the IEEE/CVF conference on computer vision and pattern recognition*. pp. 5728–5739 (2022)

66. Zhang, Y., Li, K., Li, K., Wang, L., Zhong, B., Fu, Y.: Image super-resolution using very deep residual channel attention networks. In: Proceedings of the European conference on computer vision (ECCV). pp. 286–301 (2018)
67. Zheng, B., Pan, X., Zhang, H., Zhou, X., Slabaugh, G., Yan, C., Yuan, S.: Domainplus: Cross transform domain learning towards high dynamic range imaging. In: Proceedings of the 30th ACM International Conference on Multimedia. pp. 1954–1963 (2022)
68. Zheng, J., Li, Z., Zhu, Z., Wu, S., Rahardja, S.: Hybrid patching for a sequence of differently exposed images with moving objects. *IEEE transactions on image processing* **22**(12), 5190–5201 (2013)
69. Zimmer, H., Bruhn, A., Weickert, J.: Freehand hdr imaging of moving scenes with simultaneous resolution enhancement. *Computer Graphics Forum* **30**(2), 405–414 (2011)